The Astrophysical Journal, 909:153 (7pp), 2021 March 10 https://doi.org/10.3847/1538-4357/abddbc

The X-Ray Pulsar XTE J1858+034 Observed with NuSTAR and Fermi/GBM: Spectral and Timing Characterization plus a Cyclotron Line

C. Malacaria[1,2], P. Kretschmar[3], K. K. Madsen[4,5], C. A. Wilson-Hodge[6], Joel B. Coley[7,8], P. Jenke[9], Alexander A. Lutovinov[10], K. Pottschmidt[8,5], Sergey S. Tsygankov[11,10], and J. Wilms[12]
[1] NASA Marshall Space Flight Center, NSSTC, 320 Sparkman Drive, Huntsville, AL 35805, USA; cmalacaria@usra.edu[13]
[2] Universities Space Research Association, Science and Technology Institute, 320 Sparkman Drive, Huntsville, AL 35805, USA
[3] European Space Agency (ESA), European Space Astronomy Centre (ESAC), Camino Bajo del Castillo s/n, E-28692 Villanueva de la Caada, Madrid, Spain
[4] CRESST and X-ray Astrophysics Laboratory, NASA Goddard Space Flight Center, Greenbelt, MD 20771, USA
[5] Department of Physics and Center for Space Science and Technology, University of Maryland, Baltimore County, Baltimore, MD 21250, USA
[6] ST 12 Astrophysics Branch, NASA Marshall Space Flight Center, Huntsville, AL 35812, USA
[7] Department of Physics and Astronomy, Howard University, Washington, DC 20059, USA
[8] CRESST and Astroparticle Physics Laboratory, NASA Goddard Space Flight Center, Greenbelt, MD 20771, USA
[9] University of Alabama in Huntsville (UAH), Center for Space Plasma and Aeronomic Research (CSPAR), 301 Sparkman Drive, Huntsville, AL 35899, USA
[10] Space Research Institute of the Russian Academy of Sciences, Profsoyuznaya Str. 84/32, Moscow 117997, Russia
[11] Department of Physics and Astronomy, FI-20014, University of Turku, Finland
[12] Remeis-Observatory and Erlangen Centre for Astroparticle Physics, Friedrich-Alexander-Universität Erlangen-Nürnberg, Sternwartstr. 7, D-96049 Bamberg, Germany
Received 2020 November 4; revised 2021 January 11; accepted 2021 January 18; published 2021 March 15

Abstract

Accreting X-ray pulsars (XRPs) undergo luminous X-ray outbursts during which the spectral and timing behavior of the neutron star can be studied in detail. We analyze a NuSTAR observation of the XRP XTE J1858+034 during its outburst in 2019. The spectrum is fit with a phenomenological, a semiempirical, and a physical spectral model. A candidate cyclotron line is found at 48 keV, implying a magnetic field of 5.4×10^{12} G at the site of emission. This is also supported by the physical best-fit model. We propose an orbital period of about 81 days based on the visual inspection of the X-ray outburst recurrence time. Based on Fermi/GBM data, the standard disk accretion-torque theory allowed us to infer a distance of 10.9 ± 1.0 kpc. Pulse profiles are single-peaked and show a pulsed fraction that is strongly energy-dependent at least up to 40 keV.

Unified Astronomy Thesaurus concepts: X-ray binary stars (1811); Neutron stars (1108); Pulsars (1306); Accretion (14); Stellar accretion disks (1579); Magnetic fields (994)

1. Introduction

Accreting X-ray pulsars (XRPs) are binary systems consisting of a neutron star (NS) that accretes matter originating from a donor companion star via stellar wind or Roche-lobe overflow. The XRP XTE J1858+034 was discovered with the Rossi X-ray Timing Explorer in 1998 by Remillard et al. (1998) and Takeshima et al. (1998). Those observations also detected X-ray pulsations with a period of ∼221 s. The X-ray emission from this source has been detected only in a few short outbursts (Nakajima et al. 2019 and references therein), thus preventing the obtaining of an orbital solution or in-depth characterization of the system. A cyclotron resonant scattering feature (CRSF) also has not been observed from this source so far. When observed, the energy $E_{\rm cyc}$ of the fundamental CRSF probes the magnetic field strength at the site of spectral emission, $E_{\rm cyc} \sim 11.6 \times B_{12}(1+z_{\rm g})^{-1}$ keV, where B_{12} is the magnetic field in units of 10^{12} G, and $z_{\rm g}$ is the gravitational redshift (see Staubert et al. 2019 for a recent review). However, Paul & Rao (1998) estimated a magnetic field strength of $0.8 \times 10^{12} \times d_{\rm kpc}$ G (with $d_{\rm kpc}$ the distance value in units of kiloparsecs) based on the observation of quasiperiodical oscillations in this system.

Reig et al. (2004, 2005) proposed a Be-type star for the optical counterpart, for which neither the spectral subtype nor the distance was found. This star was the only one within the hard X-ray error circle from INTEGRAL observations (Molkov et al. 2004) showing Hα emission and was thus proposed as counterpart, although it lay outside the error circle of the JEM-X soft X-ray instrument. At an angular offset of 3.″5 from the nominal X-ray source position, Gaia found an optical candidate counterpart (Bailer-Jones et al. 2018), mentioned in Malacaria et al. (2020) as a possible counterpart but likely unassociated given the large offset. In addition, the Gaia counterpart is at an angular offset of 103″ from, and thus clearly not associated with, the optical counterpart proposed by Reig et al. (2005). This question is discussed in more detail in the accompanying paper by Tsygankov et al. (2021), who identified a counterpart based on Chandra and ground telescope observations with a probable distance of 7–14 kpc.

Recently, the source underwent a new outburst episode (Nakajima et al. 2019) and was observed with NuSTAR. Here we study its spectral and timing characteristics and finally form a consistent general overview for the X-ray behavior of XTE J1858+034, including a distance estimate based on accretion-torque theory. The analysis presented here is complemented by the work in the accompanying paper by Tsygankov et al. (2021).

2. Data Reduction

NuSTAR (Harrison et al. 2013) was launched in 2012. It is currently the only X-ray mission with a telescope able to focus hard X-rays above 10 keV. NuSTAR consists of two identical coaligned telescopes that focus X-ray photons onto two independent focal plane modules, FPMA and FPMB. At the

[13] NASA Postdoctoral Fellow.

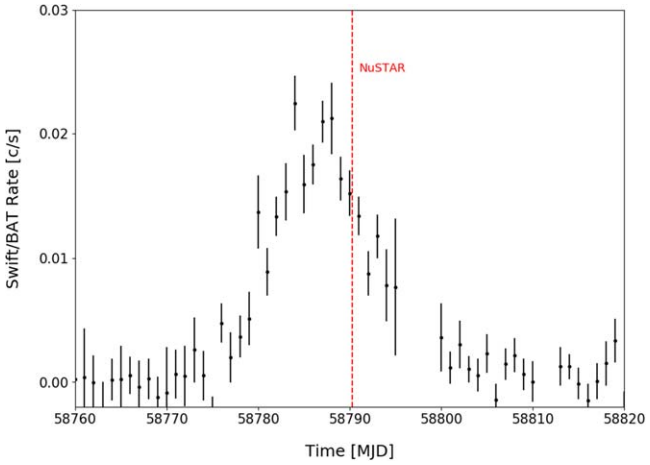

Figure 1. Swift/BAT daily average light curve of XTE J1858+034 during the outburst in 2019 (black dots). The NuSTAR observation time is also shown (red dashed line).

focus of each telescope module are four (2×2) solid-state cadmium zinc telluride (CdZnTe) imaging detectors. These provide wideband (3–79 keV) energy coverage with an FWHM of 18″ and a spectral resolution of 400 eV at 10 keV.

NuSTAR observed XTE J1858+034 on 2019 November 3 (ObsID 90501348002, MJD 58,790), during an outburst (see Figure 1). The total exposure time was about 44 ks. The NuSTAR data were reduced with `NUSTARDAS` v1.9.5 provided by `HEASOFT` v6.27.2 and using CALDB 20200526 (Madsen et al. 2020). Cleaned events were obtained following the standard NuSTAR guidelines. The resulting images are shown in Figure 2. Source spectra were extracted through the `NUPRODUCTS` routine. The source extraction region was a 65″ radius circular region centered on the source, while the background was extracted from a source-free region on the same detector with radii of 90″ and 105″ for FPMA and FPMB, respectively. We also verified that shifting the extraction regions in order to account for the offset between the images from the two modules does not significantly affect the results. However, in the FPMB part of the source, events fall on the chip gap between detectors 0 and 3, resulting in an unaccounted loss of effective area. Moreover, the NuSTAR detectors suffer from absorption due to a CdZnTe dead layer and a Pt coating at the top of the detectors, an effect that is calibrated through observations of the Crab in stray-light mode (Madsen et al. 2017). However, the absorption curve can be degenerate with other effective area effects, and for detector 3, this has caused part of the detector-related absorption to be included in the vignetting curve, thus resulting in spectral differences in the low-energy spectrum when compared to detector 0 (private communication with the NuSTAR Science Operations Team). All of these factors led us to exclude the entire detector 3 from the FPMB source extraction region. We obtained the FPMB Ancillary Response File (ARF) from a 15″ radius circular region centered on the source, which ensures that the detector absorption of detector 3 did not get included. Similarly, to avoid accidentally including the Response Matrix File (RMF) from detector 3 during RMF generation, the RMF for detector 0 was obtained directly from CALDB (`nuBcutdet0_20100101v001`).

Spectral data were analyzed using `XSPEC` v12.11.01 (Arnaud 1996). NuSTAR data were used in the range 3–60 keV (3.5–60 keV for FPMB to further enhance the consistency between spectra in the lowest channels), above which the background dominates. Spectra were rebinned to have at least 50 counts bin^{-1}.

3. Results

3.1. Spectral Analysis

As observed by NuSTAR in 2019 November, XTE J1858+034 clearly shows a hard spectrum. The FPMA and FPMB spectra have been fitted simultaneously, allowing for a cross-normalization factor. Although the cross-normalization factor between FPMA and FPMB is usually of the order of a few percent (Madsen et al. 2015), the limited ARF extraction region adopted in our analysis for FPMB (see Section 2) is expected to reduce the cross-normalization value significantly. For the spectral fit, standard phenomenological and semiempirical continuum models have been employed, namely, two variants of the cutoff power-law model (`cutoffpl` and `highecut * pow` in `XSPEC`) and a Comptonization model of soft photons in a hot plasma (`compTT` in `XSPEC`; Titarchuk 1994), respectively. To obtain an acceptable fit, the `cutoffpl` and `highecut * pow` models need an additional component in the lower energy band, which has been modeled as a blackbody emission as found in other accreting XRPs (see, e.g., La Palombara & Mereghetti 2006). However, the blackbody temperature is high with respect to other XRPs, indicating that the phenomenological model is likely inadequate. Moreover, we also tested a purely physical model of thermal and bulk Comptonization of the seed photons produced by cyclotron cooling (Ferrigno et al. 2009; `bwcycl` in `XSPEC`). For a fixed value of mass and radius of the accreting NS, the `bwcycl` model has six free parameters, namely, the accretion rate $\dot{M}$, magnetic field strength B, accretion column radius r_0, electron temperature T_e, photon diffusion parameter ξ, and Comptonization parameter δ. This model was successfully used to fit the broadband energy spectrum of a number of bright ($\gtrsim 10^{37}$ erg s^{-1}) accreting XRPs (see, e.g., Wolff et al. 2016; D'Aì et al. 2017; Epili et al. 2017).

For all tested models, the photoelectric absorption component and elemental abundances were set according to Wilms et al. (2000; `tbabs` in `XSPEC`) to account for photoelectric absorption by neutral interstellar matter (or column density N_{H}) and assuming model-relative (`wilm`) solar abundances. Given that the Galactic N_{H} in the direction of the source is about 1.7×10^{22} cm^{-2} (HI4PI Collaboration et al. 2016), all models show important local absorption values. All tested models also were equipped with a Gaussian emission line at 6.4 keV to account for the Fe Kα fluorescence emission.

All fit continuum models show absorption-like residuals in the range 40–50 keV. These residuals can be modeled with a Gaussian absorption line (see Figure 3). The improvement in the best-fit statistics is maximum in the `compTT` model, i.e., $\Delta\chi^2 = 878$. Other models show an improvement of $\Delta\chi^2 \gtrapprox 400$, with the lowest $\Delta\chi^2$ derived from the `highecut*pow` model. The significance of the line in the `compTT` model has been assessed through Monte Carlo simulations. For this task, the `XSPEC simftest` routine was adopted, which allows one to simulate a chosen number of spectra based on the actual data and test the resulting $\Delta\chi^2$ between each fit when the additional model component (the Gaussian absorption line, in our case) is included. Following Bhalerao et al. (2015) and Bodaghee et al. (2016), the column density parameter was fixed

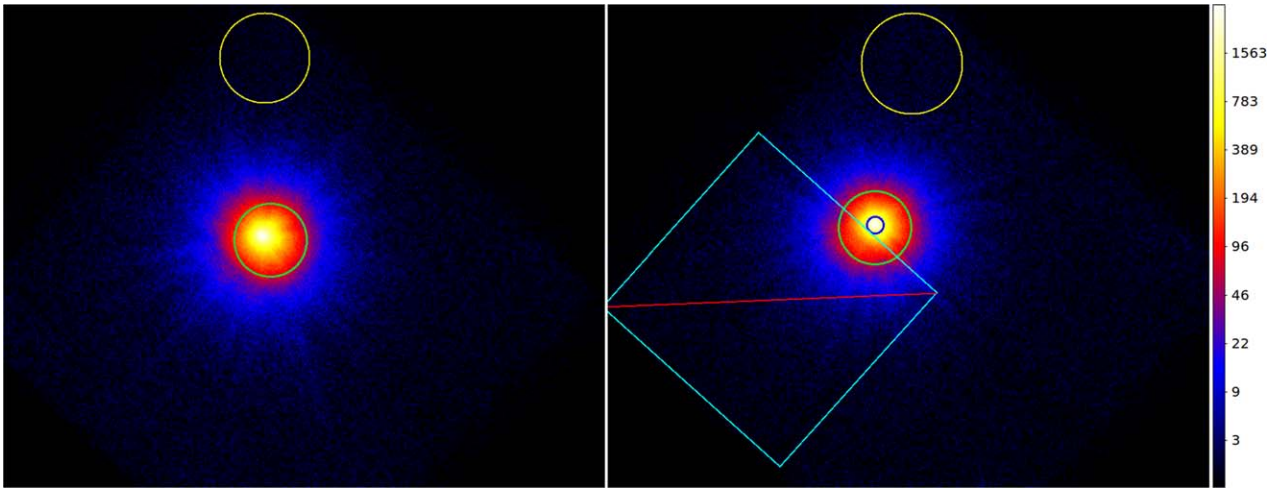

Figure 2. NuSTAR images of XTE J1858+034 as observed in 2019 November from FPMA (left) and FPMB (right). Circular green regions centered on the source represent the source extraction regions. Yellow circles at the top represent the background extraction regions. For FPMB, the small blue circle represents the ARF extraction region, while the barred cyan square represents the exclusion of detector 3 (see text). The color bar shows the number of counts per pixel.

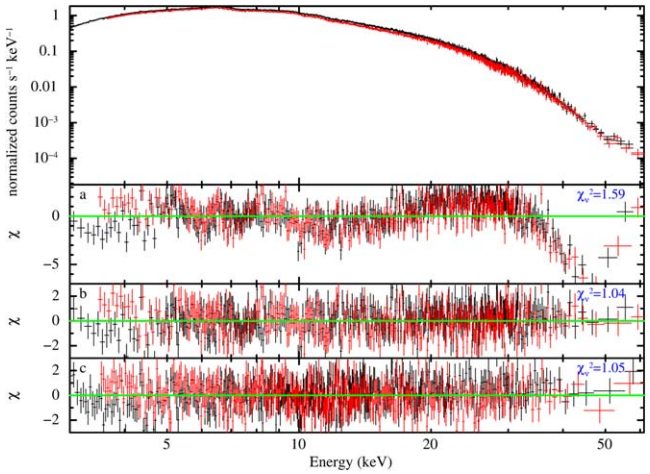

Figure 3. Top: XTE J1858+034 spectrum as observed by NuSTAR in 2019 and fit with a `comptTT` model. The bottom panels are differentiated with a letter in the upper left corner. Panel (a): residuals of the `ComptTT` model. Panel (b): residuals of the best-fit `comptTT` model, including a Gaussian absorption line at ∼48 keV (see Table 1). Panel (c): residuals of the best-fit `BWCYC IIa` model, including a Gaussian absorption line at ∼48 keV (see Table 2). Spectra and residuals have been rebinned for plotting purpose. The blue text in the upper right corners of the bottom panels shows the correspondent model χ^2 divided by ν degrees of freedom.

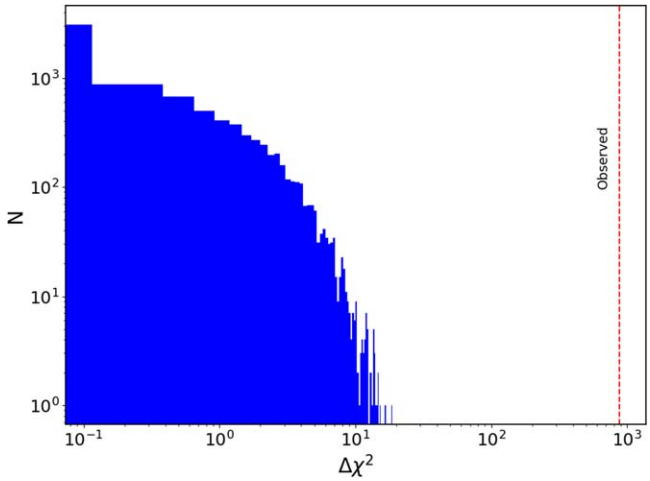

Figure 4. Results of 10,000 Monte Carlo simulations to test the significance of the Gaussian absorption line in the `compTT` model. The solid histogram shows the frequency (y-axis) of $\Delta\chi^2$ values (x-axis) obtained in the simulation. The red dashed line shows the observed $\Delta\chi^2 = 878$.

to its best-fit value, and the energy and width of the Gaussian absorption line were left free to vary within their 90% confidence region in order to improve the speed and convergence of the fits. Simulation results are reported in Figure 4 for a 10^4 iteration process and confirm the significance of the absorption feature at $>3\sigma$ c.l. Following MarcuCheatham et al. (2015), we also investigated the impact of a variable background normalization on the absorption feature parameters. Using the `XSPEC` tool `recorn`, it was found that the absorption line parameters do not change significantly if the normalization of the background spectrum is increased by up to 50%, thus strengthening the interpretation of the absorption feature as real and not due to artifacts. The feature was also observed in phase-resolved spectra presented in the accompanying paper by Tsygankov et al. (2021). Interpreting the feature at 48 keV as a CRSF and assuming a gravitational redshift of $z_g = 0.3$ (for an NS mass and radius of 1.4 $M_\odot$ and 10 km, respectively), a magnetic field strength of $B = (5.4 \pm 0.1) \times 10^{12}$ G is obtained.

Following the `bwcycl` model instructions,[14] it is convenient to freeze some of the model parameters in order to improve the computational speed and help the fit converge to the best-fit parameters. Once the best fit was found, the column density $N_{\rm H}$ was also fixed to its best-fit value to help the fit converge and obtain parameter errors. The mass and radius of the NS were fixed to their canonical values of 1.4 $M_\odot$ and 10 km, respectively. However, it is preferable to also fix the values of the NS magnetic field, its distance, and its mass accretion rate (as derived by the observed luminosity). For XTE J1858+034, there are no previous conclusive estimations of the magnetic field, while a measurement of the distance is necessary for the latter two parameters. As mentioned in Section 1, the closest Gaia counterpart to the nominal X-ray position found by Molkov et al. (2004) was unlikely to be associated with the X-ray source or the optical counterpart

[14] https://heasarc.gsfc.nasa.gov/xanadu/xspec/manual/node148.html

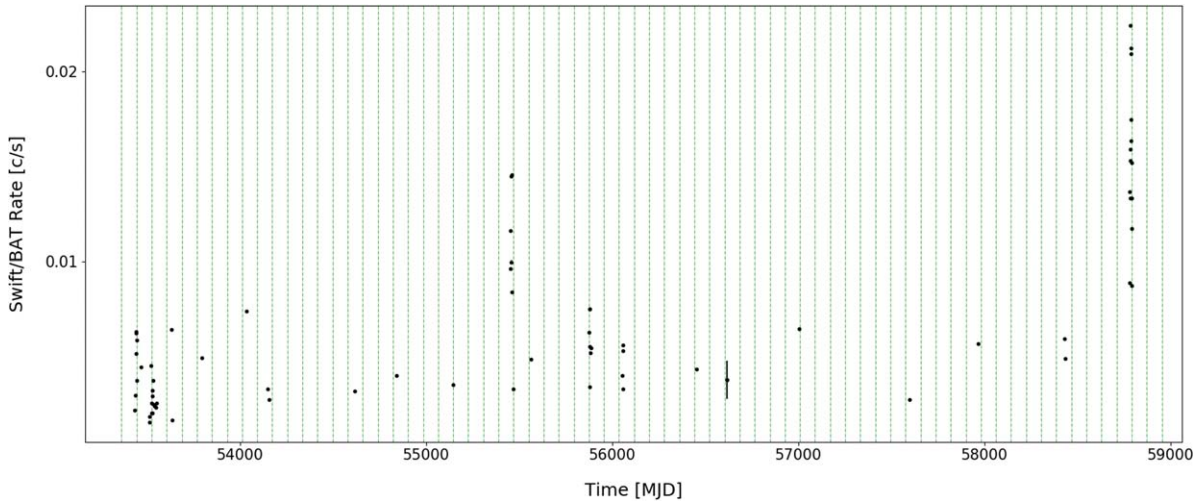

Figure 5. Swift/BAT light curve of XTE J1858+034. Only data points more significant than 3σ are reported. A typical error bar is shown for only one data point around MJD 56,500 for clarity. Green dashed–dotted lines are separated by 81 days.

proposed by Reig et al. (2005). This was ascertained by Tsygankov et al. (2021), who showed that either of those possible counterparts is consistent with the much better constrained X-ray source location available through new Chandra observations. However, the distance to the X-ray system had not been estimated before their work, which, in any case, did not constrain it very much. Therefore, we opted for a different approach to obtain a more stringent value of the distance, based on the spin-up ($\dot{P}$) measured by the Fermi Gamma-ray Burst Monitor (GBM).

To this aim, the publicly available spin-frequency values from the GBM were used.[15] The spin-up was measured during an interval of about 6 days around MJD 58,786. The resulting spin-up value is $|\dot{P}| = 10.5421(6)\ \mathrm{s\,yr^{-1}}$ (see also Malacaria et al. 2020 and references therein). Since the orbital parameters of this system are unknown, we tested the contribution of orbital modulation to the observed spin-up. First, although Doroshenko et al. (2008) reported a possible orbital period for this source of about 380 days, we notice that its significance is low, while a visual inspection of the Swift/BAT (Krimm et al. 2013) data[16] for this source revealed an outburst recurrence of ∼81 days (see Figure 5), here assumed as the orbital period. Moreover, for a K- or M-type optical companion star (Tsygankov et al. 2021), we adopted a value of the mass function $f(M) = M_*{}^3 \sin^3 i/(M_* + M_{\rm NS})^2 = 1$, where M_* and $M_{\rm NS}$ are the mass of the companion and NS, respectively, and i is the binary system inclination. This corresponds to a value of the semimajor projected axis, $a_x \sin i \simeq 190$ lt-s. Also, the data required only a small value of the eccentricity, assumed here as $e \simeq 0.1$. Finally, an epoch of $T_0 = 53{,}436$ MJD was chosen at the beginning of the first of the recurring outbursts. An argument of periapse of $\omega = 107°$ was found to best fit the GBM frequency values assuming no accretion torque. This orbit assumed, the maximum orbital contribution to the spin-up was found to be only about 10%.

Assuming a magnetic field strength of 5.4×10^{12} G and adopting the NuSTAR measured flux of 1.5×10^{-9} erg cm^{-2} s^{-1} (see Tables 1 and 2), the standard accretion-disk torque theory (Ghosh & Lamb 1979) can be used to infer the distance of the source according to the equation

$$-\dot{P} = 5 \times 10^{-5}\ \mathrm{s\,yr^{-1}}\, M_{1.4}^{-3/7}\, R_6^{6/7}\, I_{45}^{-1} \times n(\omega_s)\mu_{30}^{2/7}(P\, L_{37}^{3/7})^2, \quad (1)$$

where $M_{1.4}$ is the NS mass in units of $1.4\,M_\odot$, R_6 is the NS radius in units of 10^6 cm, I_{45} is the moment of inertia in units of 10^{45} g cm^2, μ_{30} is the magnetic moment in units of 10^{30} G cm^3, $n(\omega_s) \approx 1.4$ is the dimensionless torque, P is the spin

Table 1
Best-fit Results of XTE J1858+034 Spectral Analysis with a Cutoff Power-law Model `cutoffpl` and a Comptonization Model `compTT`

	cutoffpl	compTT
$C_{\rm FPMB}$	$0.747^{+0.001}_{-0.001}$	$0.747^{+0.001}_{-0.001}$
$N_{\rm H}$ (10^{22} cm^{-2})	$7.6^{+0.4}_{-0.4}$	$5.8^{+0.3}_{-0.3}$
$kT_{\rm bb}$ (keV)	$5.2^{+0.2}_{-0.1}$	…
$\mathrm{Norm_{bb}}$	$0.0152^{+0.0002}_{-0.0007}$	…
$E_{\rm K\alpha}$ (keV)	$6.47^{+0.02}_{-0.02}$	$6.48^{+0.02}_{-0.02}$
$\sigma_{\rm K\alpha}$ (keV)	$0.26^{+0.02}_{-0.02}$	$0.28^{+0.02}_{-0.02}$
$\mathrm{Norm_{K\alpha}}$ (10^{-4})	$5.5^{+0.4}_{-0.4}$	$5.9^{+0.4}_{-0.4}$
Γ	$0.03^{+0.29}_{-0.22}$	…
`highecut` (keV)	$3.5^{+1.5}_{-0.5}$	…
$\mathrm{Norm_\Gamma}$[a]	$0.025^{+0.006}_{-0.004}$	…
T_0 (keV)	…	$1.02^{+0.02}_{-0.02}$
$kT_{\rm compTT}$ (keV)	…	$5.61^{+0.05}_{-0.04}$
$\tau_{\rm p}$ (keV)	…	$7.07^{+0.06}_{-0.06}$
$\mathrm{Norm_{compTT}}$	…	$0.0228^{+0.0003}_{-0.0003}$
$E_{\rm gabs}$ (keV)	$46.8^{+1.0}_{-0.8}$	$48.0^{+0.8}_{-0.7}$
$\sigma_{\rm gabs}$ (keV)	$7.7^{+1.0}_{-0.7}$	$8.6^{+0.6}_{-0.5}$
Strength gabs	$14.9^{+5.1}_{-2.6}$	$21.3^{+2.0}_{-2.5}$
Flux[b]	$1.499^{+0.003}_{-0.003}$	$1.499^{+0.003}_{-0.003}$
χ^2/dof	1645/1574	1643/1573

Notes. All reported errors are at 1σ c.l.
[a] In units of photons^{-1} keV^{-1} cm^{-2} s^{-1} at 1 keV.
[b] Flux calculated for the entire model in the 3–60 keV band and reported in units of 10^{-9} erg cm^{-2} s^{-1}. Flux values with estimated errors were derived using the `cflux` model from `XSPEC` as resulting from FPMA.

[15] https://gammaray.nsstc.nasa.gov/gbm/science/pulsars/lightcurves/xtej1858.html
[16] https://swift.gsfc.nasa.gov/results/transients/weak/XTEJ1858p034/

Table 2
Best-fit Results of XTE J1858+034 Spectral Analysis with Different Configurations of the Physical Bulk+Thermal Comptonization Model `bwcyc`

	BWCYCa	BWCYCb	BWCYCc
$C_{\rm FPMB}$	$0.748^{+0.001}_{-0.001}$	$0.748^{+0.001}_{-0.001}$	$0.748^{+0.001}_{-0.001}$
$N_{\rm H}$ (10^{22} cm^{-2})	$8.6^{+0.2}_{-0.2}$	$8.4^{+0.2}_{-0.2}$	$8.4^{+0.3}_{-0.8}$
$E_{\rm K\alpha}$ (keV)	$6.47^{+0.02}_{-0.02}$	$6.48^{+0.02}_{-0.02}$	$6.47^{+0.02}_{-0.02}$
$\sigma_{\rm K\alpha}$ (keV)	$0.27^{+0.02}_{-0.02}$	$0.28^{+0.02}_{-0.02}$	$0.27^{+0.02}_{-0.02}$
Norm$_{\rm K\alpha}$ (10^{-4})	$5.5^{+0.4}_{-0.4}$	$5.6^{+0.3}_{-0.3}$	$5.6^{+0.4}_{-0.4}$
ξ	$4.2^{+0.7}_{-1.7}$	$3.2^{+0.8}_{-0.8}$	$2.9^{+1.0}_{-0.6}$
δ	$0.4^{+0.3}_{-0.1}$	$0.6^{+0.3}_{-0.1}$	$0.7^{+0.3}_{-0.2}$
B (10^{12} G)	$4.4^{+0.5}_{-0.3}$	5.4 (fixed)	5.4 (fixed)
$\dot{M}$ (10^{17} g s^{-1})	1.2 (fixed)	1.2 (fixed)	$1.1^{+0.1}_{-0.1}$
T_e (keV)	$5.6^{+0.2}_{-0.6}$	$5.5^{+0.1}_{-0.5}$	$5.2^{+0.2}_{-0.4}$
r_0 (m)	73^{+9}_{-22}	66^{+22}_{-12}	49^{+29}_{-10}
d (kpc)	10.9 (fixed)	10.9 (fixed)	10.9 (fixed)
$E_{\rm gabs}$ (keV)	$48.3^{+0.7}_{-0.7}$	$48.6^{+0.5}_{-1.3}$	$48.3^{+1.0}_{-1.1}$
$\sigma_{\rm gabs}$ (keV)	$10.3^{+0.7}_{-2.1}$	$9.6^{+1.2}_{-1.2}$	$9.3^{+1.3}_{-0.6}$
Strength$_{\rm gabs}$	$25.4^{+4.2}_{-6.4}$	$27.6^{+3.1}_{-4.2}$	$25.3^{+4.0}_{-3.9}$
Flux[b]	$1.499^{+0.003}_{-0.003}$	$1.499^{+0.003}_{-0.002}$	$1.499^{+0.003}_{-0.003}$
χ^2/dof	1648/1574	1648/1575	1648/1574

Notes. All reported errors are at 1σ c.l.
[a] Unconstrained.
[b] Flux calculated in the 3–60 keV band and reported in units of 10^{-9} erg cm^{-2} s^{-1}. Flux values with estimated errors were derived using the `cflux` model from `XSPEC` as calculated for FPMA.

period in seconds, and L_{37} is the bolometric luminosity in units of 10^{37} erg s^{-1}. For a measured $|\dot{P}| = 10.5$ s yr^{-1}, Equation (1) allows one to infer a distance of $d = 10.9 \pm 1.0$ kpc (estimated uncertainty at 1σ c.l.). This distance value is also independently confirmed by the analysis of the optical companion star, as reported in the accompanying paper by Tsygankov et al. (2021), and it was used to characterize different configurations of the `bwcyc` model. The corresponding mass accretion rate $\dot{M} = 1.2 \times 10^{17}$ g s^{-1} was adopted altogether, derived assuming a luminosity $L = \eta \dot{M} c^2$ with efficiency $\eta = 0.2$ (Sibgatullin & Sunyaev 2000). The different configurations of the tested model are reported in Table 2, including a set with the magnetic field strength as a free parameter (`BWCYCa`), one with the magnetic field strength fixed to 5.4×10^{12} G (`BWCYCb`), and one with a free $\dot{M}$ and fixed magnetic field strength (`BWCYCc`).

3.2. Timing Analysis

For the timing analysis, the `nuproducts` task was used to obtain light curves out of calibrated and cleaned events. These light curves were corrected for live-time, exposure, and vignetting effects and extracted in the following energy bands: 3–10, 10–20, 20–30, 30–40, 40–60, and 3–60 keV.

All light curves were barycentered using the `barycorr` tool and the NuSTAR clock correction file `nuCclock20100101v103`. The light curve in the 3–60 keV energy band was binned to 5 s and used to search for pulsations around the known 221 s periodicity with the epoch folding method (Leahy 1987). The procedure results in a measured period of $P = 218.393(2)$ s. Pulsations are significant at >99%.

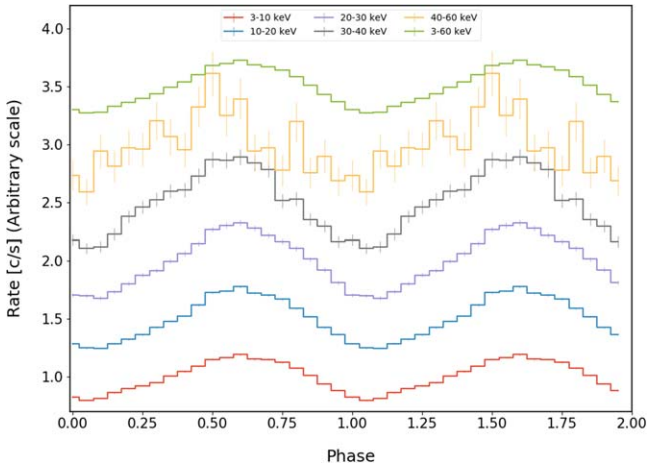

Figure 6. The XTE J1858+034 energy-resolved pulse profiles as observed by NuSTAR. The energy band increases upward. Pulse profiles are shown twice in phase and rescaled in count rate for clarity.

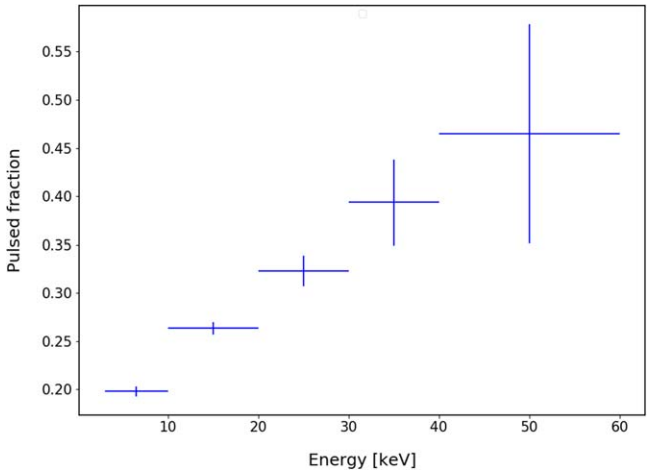

Figure 7. The XTE J1858+034 pulsed fraction as a function of the energy during the NuSTAR observation in 2019 November.

The uncertainty was estimated by simulating 500 light curves based on real data and altered with Poisson noise.

Light curves in different energy bands were folded to the best-fit spin period to obtain pulse profiles with a resolution of 20 phase bins (see Figure 6). In turn, these were used to explore the pulsed fraction variation as a function of the energy (see Figure 7). The pulsed fraction here is defined as $(I_{\rm max} - I_{\rm min})/(I_{\rm max} + I_{\rm min})$, where $I_{\rm max}$, $I_{\rm min}$ are the maximum and minimum pulse profile count rate, respectively.

4. Discussion

4.1. Thermal Comptonization and a Candidate Cyclotron Line

The hard spectrum of XTE J1858+034 resembles that of other accreting XRPs observed at both low and high luminosity and well fit by a `compTT` model (Mukerjee et al. 2020 and references therein). The observation of `compTT` spectra in accreting XRPs is usually interpreted as the result of thermal Comptonization processes in which the thermal energy of the accreting gas is transferred to the seed photons originating from the NS hot spots (Becker & Wolff 2007). An increasing number of these sources also show that an additional `compTT` component emerges in the high-energy range of the spectrum at

low-luminosity stages (Tsygankov et al. 2019a, 2019b). Although the formation of such a component is not clear yet, it is likely due to a combination of cyclotron emission and following thermal Comptonized emission from a thin overheated layer of the NS atmosphere (see Tsygankov et al. 2019b, and references therein). In this context, X Persei is a remarkable case, since it has been shown that the cyclotron line in its spectrum can be mimicked by the convolution of the two compTT spectral components around the energy where the flux from the low- and high-energy components is comparable (Doroshenko et al. 2012). However, among the sources whose spectrum is formed by two compTT components, X Persei is the one with the highest electron temperature of the hard-energy compTT component, $kT \sim 15$ keV. If the absorption feature at ~48 keV in XTE J1858+034 does in fact result from the blend of two compTT components, the high-energy compTT would peak around 22 keV. This would make XTE J1858+034 the most extreme among the XRPs that show such a spectral shape. However, such a spectral shape has so far only been observed in low-luminosity XRPs, while our analysis (see Section 3.1) shows that the source is located at a relatively large distance of 10.9 kpc, thus implying a high-luminosity source (also supported by the analysis of Tsygankov et al. 2021). A second Gaussian or compTT component that peaked above 45 keV was also tested in place of the absorption feature but could not be successfully fit ($\chi^2_{\rm red} > 1.4$), possibly due to the lack of statistics above 60 keV.

4.2. Thermal and Bulk Comptonization

With the newly inferred source distance value of $d = 10.9$ kpc, the derived flux of 1.5×10^{-9} erg cm^{-2} s^{-1} implies a luminosity of 2.1×10^{37} erg s^{-1}. Adopting this distance value, all different sets of the bwcyc model are statistically equivalent, and all parameters show acceptable values. For the BWCYCa configuration, the returned magnetic field strength of 4.2×10^{12} G is consistent within 2σ with that inferred from the candidate CRSF. Notably, the BWCYCb model with fixed values of the distance, magnetic field strength, and accretion rate also fits the data and returns acceptable values of the best-fit parameters. The BWCYCc fit returns the smallest (but still acceptable) r_0 value and a mass accretion rate $\dot{M}$ that is almost coincident with that inferred from the X-ray (isotropic) luminosity.

In any case, when interpreting the results from the bwcyc model, it is important to keep in mind that, as reported in Ferrigno et al. (2009), the BWcyc model may need adjustments in the spectral parameters with respect to the original prescriptions. For example, the best-fit magnetic field value may differ from that inferred by the CRSF if the spectrum is formed at an NS site that is spatially different from the CRSF-forming region. Likewise, the best-fit mass accretion rate $\dot{M}$ can be different from that inferred by the X-ray luminosity due to an uncertain efficiency conversion factor (η) and anisotropic emission.

4.3. Timing Results

The pulse profiles of XTE J1858+034 as observed by NuSTAR show a single-peak structure and a shape that is only weakly energy-dependent (see Figure 6). This is typically observed at low mass accretion rates (see, e.g., Malacaria et al. 2015) and qualitatively interpreted as the beaming pattern resulting from a pencil-beam emission. However, single-peaked pulse profiles are also observed at high accretion rates, like in the case of pulsating ultraluminous X-ray sources, e.g., Swift J0243.6+6124, where single-peak pulse profiles persist at high luminosity and only switch to more complex profiles at super-Eddington luminosity (Wilson-Hodge et al. 2018).

The pulsed fraction shows a considerable energy dependence and almost doubles from 20% in the 3–10 keV energy band to about 40% in the 30–40 keV energy band, above which the lack of statistics prevents us from drawing firm conclusions.

5. Conclusions

We analyzed the NuSTAR observation of the 2019 outburst of the XRB XTE J1858+034. The source, relatively poorly studied, has now been characterized in multiple ways. A candidate cyclotron line is found in its spectrum at 48 keV. This implies a magnetic field strength of 5.4×10^{12} G, consistent with the value obtained from the physical fitting model of thermal and bulk Comptonization bwcyc in its best-fit configurations. We propose an orbital period of about 81 days based on the visual inspection of the X-ray outburst recurrence time. Arguments are given to review the previously proposed optical counterpart and its distance value in favor of a distance of 10.9 ± 1.0 kpc obtained from standard accretion-torque theory.

This research has made use of data and software provided by the High Energy Astrophysics Science Archive Research Center (HEASARC), which is a service of the Astrophysics Science Division at NASA/GSFC and the High Energy Astrophysics Division of the Smithsonian Astrophysical Observatory. We acknowledge extensive use of the NASA Abstract Database Service (ADS). C.M. is supported by an appointment to the NASA Postdoctoral Program at the Marshall Space Flight Center, administered by the Universities Space Research Association under contract with NASA. The contribution by K.P. is supported by NASA under award number 80GSFC17M0002. A.A.L. and S.S.T. acknowledge support from the Russian Science Foundation (grant 19-12-00423).

ORCID iDs

C. Malacaria https://orcid.org/0000-0002-0380-0041
P. Kretschmar https://orcid.org/0000-0001-9840-2048
K. K. Madsen https://orcid.org/0000-0003-1252-4891
C. A. Wilson-Hodge https://orcid.org/0000-0002-8585-0084
Joel B. Coley https://orcid.org/0000-0001-7532-8359
Alexander A. Lutovinov https://orcid.org/0000-0002-6255-9972
K. Pottschmidt https://orcid.org/0000-0002-4656-6881
Sergey S. Tsygankov https://orcid.org/0000-0002-9679-0793
J. Wilms https://orcid.org/0000-0003-2065-5410

References

Arnaud, K. A. 1996, in ASP Conf. Ser. 101, Astronomical Data Analysis Software and Systems V, ed. G. H. Jacoby & J. Barnes (San Francisco, CA: ASP), 17
Bailer-Jones, C. A. L., Rybizki, J., Fouesneau, M., Mantelet, G., & Andrae, R. 2018, AJ, 156, 58
Becker, P. A., & Wolff, M. T. 2007, ApJ, 654, 435
Bhalerao, V., Romano, P., Tomsick, J., et al. 2015, MNRAS, 447, 2274

Bodaghee, A., Tomsick, J. A., Fornasini, F. M., et al. 2016, ApJ, 823, 146
D'ìA, A., Cusumano, G., DelSanto, M., LaParola, V., & Segreto, A. 2017, MNRAS, 470, 2457
Doroshenko, V., Santangelo, A., Kreykenbohm, I., & Doroshenko, R. 2012, A&A, 540, L1
Doroshenko, V. A., Doroshenko, R. F., Postnov, K. A., Cherepashchuk, A. M., & Tsygankov, S. S. 2008, ARep, 52, 138
Epili, P., Naik, S., Jaisawal, G. K., & Gupta, S. 2017, MNRAS, 472, 3455
Ferrigno, C., Becker, P. A., Segreto, A., Mineo, T., & Santangelo, A. 2009, A&A, 498, 825
Ghosh, P., & Lamb, F. K. 1979, ApJ, 234, 296
Harrison, F. A., Craig, W. W., Christensen, F. E., et al. 2013, ApJ, 770, 103
HI4PI Collaboration, Ben Bekhti, N., Flöer, L., et al. 2016, A&A, 594, A116
Krimm, H. A., Holland, S. T., Corbet, R. H. D., et al. 2013, ApJS, 209, 14
La Palombara, N., & Mereghetti, S. 2006, A&A, 455, 283
Leahy, D. A. 1987, A&A, 180, 275
Madsen, K. K., Forster, K., Grefenstette, B. W., Harrison, F. A., & Stern, D. 2017, ApJ, 841, 56
Madsen, K. K., Grefenstette, B. W., Pike, S., et al. 2020, arXiv:2005.00569
Madsen, K. K., Harrison, F. A., Markwardt, C. B., et al. 2015, ApJS, 220, 8
Malacaria, C., Jenke, P., Roberts, O. J., et al. 2020, ApJ, 896, 90
Malacaria, C., Klochkov, D., Santangelo, A., & Staubert, R. 2015, A&A, 581, A121
MarcuCheatham, D. M., Pottschmidt, K., Kühnel, M., et al. 2015, ApJ, 815, 44
Molkov, S. V., Cherepashchuk, A. M., Revnivtsev, M. G., et al. 2004, ATel, 274, 0
Mukerjee, K., Antia, H. M., & Katoch, T. 2020, ApJ, 897, 73
Nakajima, M., Negoro, H., Kurogi, K., et al. 2019, ATel, 13217, 1
Paul, B., & Rao, A. R. 1998, A&A, 337, 815
Reig, P., Kougentakis, T., & Papamastorakis, G. 2004, ATel, 308, 0
Reig, P., Negueruela, I., Papamastorakis, G., Manousakis, A., & Kougentakis, T. 2005, A&A, 440, 637
Remillard, R., Levine, A., Takeshima, T., et al. 1998, IAUC, 6826, 0
Sibgatullin, N. R., & Sunyaev, R. A. 2000, AstL, 26, 699
Staubert, R., Trümper, J., Kendziorra, E., et al. 2019, A&A, 622, A61
Takeshima, T., Corbet, R. H. D., Marshall, F. E., Swank, J., & Chakrabarty, D. 1998, IAUC, 6826, 1
Titarchuk, L. 1994, ApJ, 434, 570
Tsygankov, S. S., Doroshenko, V., Mushtukov, A. A., et al. 2019a, MNRAS, 487, L30
Tsygankov, S. S., Lutovinov, A. A., Molkov, S. V., et al. 2021, ApJ, 909, 154
Tsygankov, S. S., Rouco Escorial, A., Suleimanov, V. F., et al. 2019b, MNRAS, 483, L144
Wilms, J., Allen, A., & McCray, R. 2000, ApJ, 542, 914
Wilson-Hodge, C. A., Malacaria, C., Jenke, P. A., et al. 2018, ApJ, 863, 9
Wolff, M. T., Becker, P. A., Gottlieb, A. M., et al. 2016, ApJ, 831, 194